

ARTICLE OPEN



Oxidation behavior of Cr-coated zirconium alloy cladding in high-temperature steam above 1200 °C

Hai-Bin Ma¹, Jun Yan¹, Ya-Huan Zhao¹, Tong Liu^{1✉}, Qi-Sen Ren¹, Ye-Hong Liao¹, Jia-Dong Zuo², Gang Liu^{2✉} and Mei-Yi Yao³

Dense, uniform, and well-adhered chromium (Cr) coatings were deposited on zirconium (Zr) alloy claddings by using physical vapor deposition (PVD). The Cr-coated samples were tested at 1200 °C and 1300 °C, respectively, for different exposure time in water steam environment. Microstructures and compositions of the coating/substrate system after oxidation were characterized by X-ray diffraction, scanning electronic microscopy, and energy dispersion spectrometer. The microstructural results clearly demonstrated that Cr₂O₃ layer has been produced on the coating surface, acting as an oxygen diffusion barrier and concomitantly reducing the oxidation rate. The experimental results on weight gains soundly supported the microstructural findings that the Cr coatings could protect the Zr substrate from high-temperature steam oxidation, even at a temperature up to 1300 °C. Finally, the oxidation kinetics was theoretically analyzed and the underlying oxidation mechanism was also clarified.

npj Materials Degradation (2021)5:7; <https://doi.org/10.1038/s41529-021-00155-8>

INTRODUCTION

The Fukushima-Daiichi nuclear accident in Japan caused by earthquake and tsunami in 2011 has drawn worldwide attention to power plant safety under accident conditions. Zirconium alloy (Zr alloy) fuel claddings have been long used in light water reactors (LWR). However, the Zr alloys will be oxidized rapidly with steam to produce a large quantity of exothermal energy and hydrogen at the loss of coolant accident (LOCA) scenario. After this nuclear accident, accident tolerant fuel (ATF) development programs were started in many countries^{1–4}. Compared with the current UO₂ (pallet)-Zr (cladding) system, ATF is a new fuel pallet-cladding that could improve the safety of the fuel assemblies beyond the design basis accident (DBA). At the same time, the performance of fuel assemblies under normal operational conditions could be maintained or enhanced in the application of ATF. Basically, the ATF concepts involve pallet and cladding. Therefore, the major potential approaches for the development of ATF are improving pallet or cladding properties. And several candidate fuels and claddings have been designed and investigated⁵.

The potential fuels mainly include high-performance UO₂ (Cr₂O₃-doped UO₂, BeO-doped UO₂, etc.), high-density fuels (U₃Si₂, UN, etc.) and fully ceramic micro-encapsulated fuels⁵. The potential claddings mainly include coated zirconium alloy^{6–9}, refractory metal¹⁰, advanced steels^{11–13}, and SiC_f/SiC^{14–16} claddings. Among the ATF candidate materials, complete replacements of current Zr alloy with refractory metal, advanced steels or SiC_f/SiC imply a substantial evolution from the current LWR system, indicative of great difficulties and uncertainties. Although the complete replacements will offer greater potential benefit. Coated Zr alloy is introducing a protective coating on the surface of current Zr alloy cladding, which does not notably change the core physics in the reactor. Therefore, coated Zr alloy cladding requires no major design changes of the current system of LWR. Compared with other ATF candidate claddings, the coated Zr alloy is the easiest and

most economic approach, which is supposed to be the near-term choice for ATF cladding application. Some coating materials have been investigated, including pure metals^{17–20}, alloys^{21–23}, ceramics^{24,25}, and MAX phases^{8,26}, among which, the metallic Cr coatings exhibit good resistance to oxidation in both normal condition and accident condition (e.g., LOCA)^{6,17–20}. This has boosted extensive studies on the Cr-coated Zr alloy cladding during the last decade.

High-temperature oxidation tests of the Cr-coated Zr cladding have been carried out at a temperature between 800 °C and 1500 °C. The testing above 1200 °C is generally considered beyond DBA. For the binary Zr–Cr systems, 1332 °C has been identified as the low eutectic temperature, which means that Cr and Zr will form a liquid phase when heated above this temperature²⁷. Both Brachet et al.²⁸ and Oelrich et al.²⁹ have reported melting phenomena of the Cr-coated Zr cladding at temperatures higher than the eutectic point. Among the work on Cr-coated Zr claddings oxidation, to the author's knowledge, most were investigated at 1200 °C or lower^{30–32} and the exposure time was not longer than 1 h^{19,33}. The quite limited information available in literatures about the oxidation behavior at the temperature up to 1200 °C is come from Brachet et al.'s report²⁸ that one-sided oxidation testing of Cr coatings was performed at 1000, 1100, and 1200 °C for oxidation times ranging from a few minutes to a few hours. Therefore, the influence of a longer time at 1200 °C or higher temperatures on the oxidation behavior is urgently deserved to be investigated. In the present work, the oxidation behavior of Cr-coated Zr cladding prepared via physical vapor deposition (PVD) was systematically investigated at 1200 and 1300 °C for different exposure times. Microstructures and compositions of samples before and after oxidation were analyzed in detail, especially for the complicated microstructures and compositions close to the interface between the coatings and substrates. Oxidation kinetics and oxidation mechanisms were also analyzed and

¹ATF Research and Development Center, China Nuclear Power Technology Research Institute, Shenzhen, China. ²State Key Laboratory for Mechanical Behavior of Materials, Xi'an Jiaotong University, Xi'an, China. ³Institute of Materials, Shanghai University, Shanghai, China. ✉email: liutong@cgnpc.com.cn; lgsammer@xjtu.edu.cn

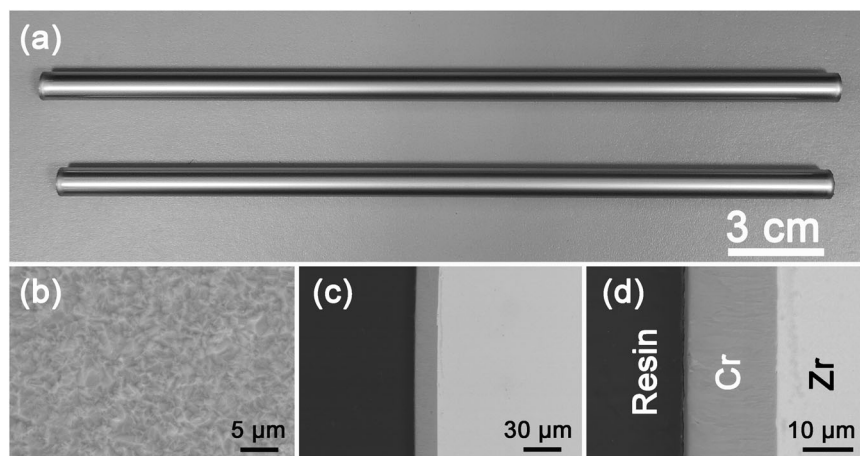


Fig. 1 Macroscopic and microscopic morphologies of the as-deposited Cr coating. **a** Sample image and SEM images of **b** surface and **c** cross-section.

discussed, which allows to understand the high temperature (HT) water steam oxidation process.

RESULTS

Coating microstructures

Figure 1 shows the photograph, surface and cross-sectional SEM images of as-deposited Cr coatings. It is identified that Cr coatings are dense without micro-cracks and well attached on the outer surface of Zr claddings. The thickness of the Cr coating is about 18 μm , which is substantially uniform along the total length, with thicknesses errors < 1 μm .

Oxidation experiments

Weight gain of the Zr tubes with or without Cr coating was comparatively measured during the whole oxidation process, and the weight gain per surface area is plotted as a function of an oxidation duration time, as shown in Supplementary Fig. 1. The weight gain of the uncoated Zr tube oxidized in 1200 $^{\circ}\text{C}$ for 1 h is about 3105 mg/dm^2 , which is nearly twice of the Cr-coated Zr tube ($\sim 1578 \text{ mg dm}^{-2}$). Since the Cr coating was produced only on the outside surface (NOT two surfaces) of the Zr cladding, one can see that the weight gain of the outer surface of Cr-coated Zr is extremely low in comparison with that of the uncoated one. The results of a weight gain are coincident with the evolution of cross-sectional microstructures, see Supplementary Figs. 2 and 3. There is no evident difference in oxide layer (ZrO_2) between the inner and the outer surfaces of the uncoated Zr tube after oxidation at 1200 $^{\circ}\text{C}$ for 1 h. However, the two surfaces of Cr-coated Zr tube exhibit quite different microstructures after oxidation. The thickness of ZrO_2 at the tube inside surface is up to $\sim 144 \mu\text{m}$ after oxidation at 1200 $^{\circ}\text{C}$ for 1 h, whereas the thickness of Cr_2O_3 at the tube outside surface is < 10 μm , as compared in Table 1. Moreover, the Cr coating after oxidation is intact and well adherent to the Zr substrate, with no spalling phenomenon found.

Structural characterization of the oxide layers

As well known, oxygen (O) can be dissolved in Zr to form brittle $\alpha\text{-Zr(O)}$ phase during the oxidation process, which will decrease the ductility of the cladding. Since the $\alpha\text{-Zr(O)}$ phase has an equiaxed morphology whereas the prior $\beta\text{-Zr}$ phase presents a lath shape in comparison, it is easy to distinguish the $\alpha\text{-Zr(O)}$ phase from the prior $\beta\text{-Zr}$ phase by comparing their

Table 1. Thickness of different layers of the Cr-coated tubes after oxidation.

Oxidation conditions	Thickness of different layers after oxidation (μm)				
	Cr_2O_3	Cr	Cr–Zr	ZrO_2 (outside)	ZrO_2 (inside)
1200 $^{\circ}\text{C}/0.5 \text{ h}$	8.4 ± 0.1	12.0 ± 0.2	1.8 ± 0.4	–	105.2 ± 3.0
1200 $^{\circ}\text{C}/1 \text{ h}$	9.5 ± 0.7	9.9 ± 0.3	2.2 ± 0.2	–	144.1 ± 4.7
1200 $^{\circ}\text{C}/2 \text{ h}$	10.2 ± 0.9	8.1 ± 0.1	3.6 ± 0.8	–	204.7 ± 4.9
1200 $^{\circ}\text{C}/4 \text{ h}$	7.8 ± 0.8	13.3 ± 0.4	$2.1^{\text{a}} \pm 0.7$	16.9 ± 1.2	312.6 ± 6.6
1300 $^{\circ}\text{C}/0.5 \text{ h}$	7.6 ± 0.7	9.7 ± 0.7	3.9 ± 1.1	–	174.3 ± 4.6
1300 $^{\circ}\text{C}/1 \text{ h}$	3.0 ± 0.3	11.8 ± 0.2	4.7 ± 0.6	5.5 ± 1.2	242.7 ± 7.5

^aThe interface between Cr and Cr–Zr layers was somewhat unclear and this value is evaluated on basis of the clear part of the Cr–Zr layer.

morphologies under the optical microscope examinations. Figure 2 shows some representative optical images of Cr-coated Zr tubes oxidized at different temperatures and times. At the oxidation conditions of 1200 $^{\circ}\text{C}/0.5 \text{ h}$, 1200 $^{\circ}\text{C}/1 \text{ h}$, and 1300 $^{\circ}\text{C}/0.5 \text{ h}$, ZrO_2 phase, $\alpha\text{-Zr(O)}$ phase, and prior $\beta\text{-Zr}$ phase are gradually present from the inner surface to the outer surface along with the coat thickness. In comparison, the prior $\beta\text{-Zr}$ phase does not exist in the other three samples that were exposed to a longer oxidation time. This means that the oxygen is ready to diffuse into the Zr substrate from the inner surface to produce a brittle $\alpha\text{-Zr(O)}$ phase. While the Cr coating can block the oxygen diffusion from the outer surface and hence decrease the oxidation rate. In the application of claddings in LWR, the claddings were welded with end plug and the inner surface will not contact the water or water steam environment. Therefore, the oxygen will not diffuse into the Zr alloy from the inner surface. By combining the weight gain results and microstructural analyses, it is proved that the Cr coating can effectively protect Zr substrate even in the high-temperature steam oxidation environment.

XRD was further performed to identify the phases in the Cr-coated and uncoated Zr claddings before and after oxidation, with results illustrated in Supplementary Fig. 4. The XRD patterns

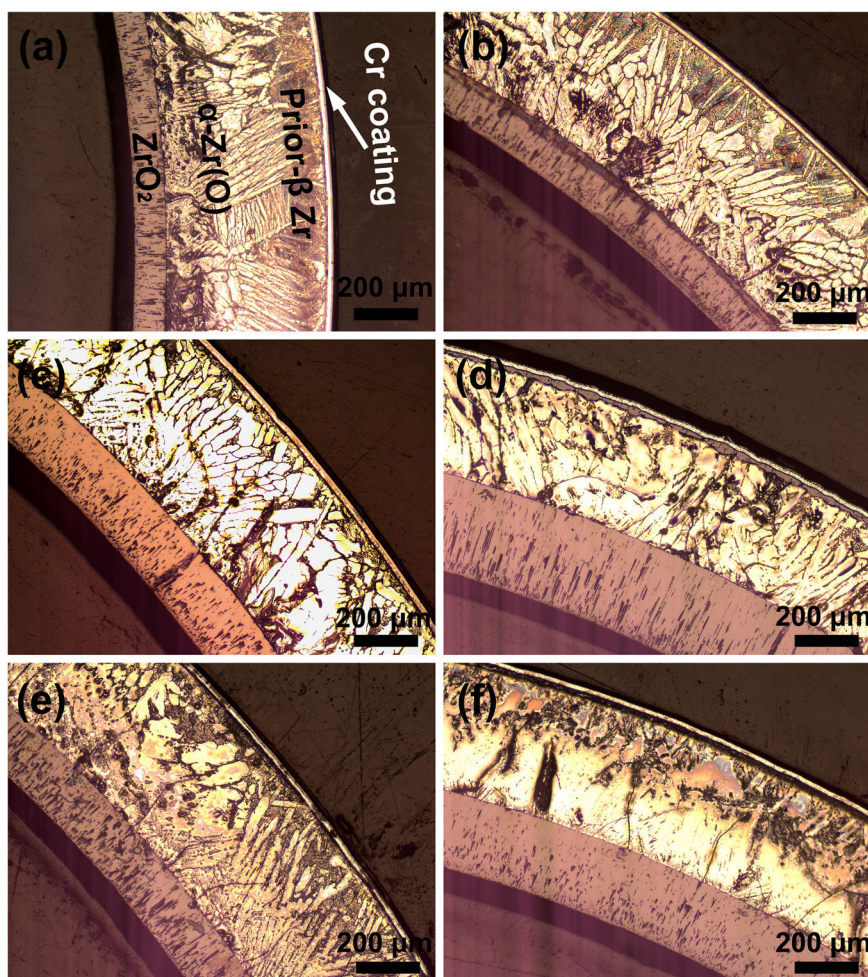
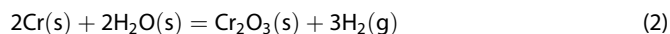
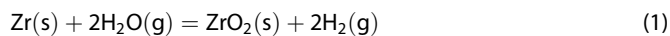


Fig. 2 Optical micrographs of the Cr-coated Zr tube oxidized at different conditions. **a** 1200 °C/0.5 h, **b** 1200 °C/1 h, **c** 1200 °C/2 h, **d** 1200 °C/4 h, **e** 1300 °C/0.5 h, **f** 1300 °C/1 h.

indicate that, after oxidation, Cr_2O_3 is present on the surface of the Cr coating and ZrO_2 has been created on the inner surface of Zr. The formation of the two oxides can be understood as follows. At high temperatures, Zr and Cr reacted with water steam according to Reactions 1 and 2.



Structural characterization of the oxide layers

Figure 3 shows surface morphologies of the Cr-coated samples after oxidation at 1200 °C and 1300 °C for different exposure times. Some whiskers and particles can be found on the surface after oxidized at 1200 °C/0.5 h and 1 h. The EDS analysis shows that the elements in them are Cr and O, and the atomic ratio of O/Cr is nearly 3/2. These indicate that the whiskers and particles are also Cr_2O_3 . Cr_2O_3 whiskers have been reported by previous studies about high-temperature steam oxidation of Cr coating, especially in the case of low oxygen potential^{34,35}. The formation of Cr_2O_3 whiskers is most possibly resulted from the rapid diffusion of Cr cations along shortcuts (e.g., grain boundaries or dislocations) in the underlying oxide film. In addition, the growth of Cr_2O_3 whiskers may be also associated with the presence of CO_2 or H_2O in the gas and it has been suggested that dissociation of these species is catalyzed at the whisker tips³⁶. In this study,

Cr_2O_3 particles in addition to whiskers were observed on the Cr coating surface. Nevertheless, in the author's opinion, their formation mechanism is thought to be the same since they both precipitated on the outmost surface and were composed of Cr_2O_3 , as stated above.

As shown in Supplementary Fig. 5a, b, these whiskers and particles look like green in color (non-uniform and discontinuous green powders exist obviously on the surface), and these powders easily fall off from the surfaces. As oxidation temperature and time increased, whiskers and particles decreased and disappeared gradually. At 1200 °C/2 h, the number of the particles is much fewer than that at 1200 °C/0.5–1 h. Correspondingly, the macroscopic morphology of Cr-coated samples of 1200 °C/2 h shows a little green color. At 1300 °C/0.5 h, the number of particles is too few to show a green appearance (Supplementary Fig. 5e). No whiskers and particles could be detected on the surface of Cr-coated samples oxidized at 1200 °C/4 h and 1300 °C/1 h. And the green powders are absent from the samples at these two oxidation conditions (Supplementary Fig. 5d, f). Obviously, the macroscopic morphologies of Cr-coated samples varied with oxidation are identical to the microstructures. Small bumps can be observed on the surfaces at the two conditions of 1200 °C/4 h and 1300 °C/1 h. The bump number density at 1200 °C/4 h is greater than at 1300 °C/1 h. However, the bump size at 1200 °C/4 h is smaller than at 1300 °C/1 h. The bumps are voids produced at the Cr_2O_3 /Cr interface region. The reason for the formation of bumps may attribute to

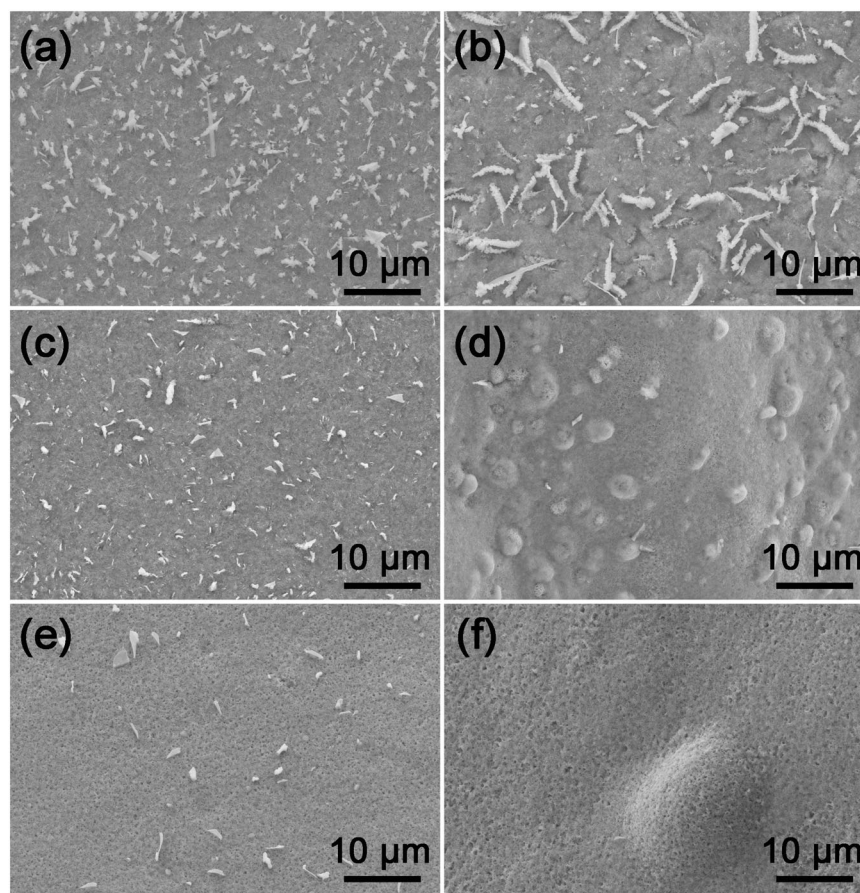
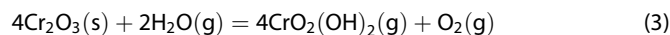


Fig. 3 SEM images showing the surface morphology of Cr-coated samples after oxidation at different conditions. **a** 1200 °C/0.5 h, **b** 1200 °C/1 h, **c** 1200 °C/2 h, **d** 1200 °C/4 h, **e** 1300 °C/0.5 h, **f** 1300 °C/1 h.

the difference in the thermal expansion of Cr_2O_3 , Cr and ZrO_2 . For the sample oxidized at 1200 °C/4 h, the time is longer. Therefore, more voids formed in the interface. At the same time, as the temperature is lower, the voids in the interface is smaller than that in the sample oxidized at 1300 °C/1 h. Small voids can be found in the Cr_2O_3 layer, as illustrated in high magnification SEM images (Supplementary Fig. 6). The voids are just on the surface of Cr_2O_3 . Since the Cr_2O_3 could continue to react with H_2O to form $\text{CrO}_2(\text{OH})_2$ (Reaction 3), the formation of voids may be attributed to the evaporation of gaseous $\text{CrO}_2(\text{OH})_2$ ³⁷. As above-mentioned, there are two reasons for the disappearance of green particles. One is that the green powders are easy to peel, and the other one is that the evaporation of $\text{CrO}_2(\text{OH})_2$.



Cross-sectional images of the outer surface of Cr-coated Zr claddings are shown in Fig. 4. The microstructures and element distributions of the samples oxidized at 1200 °C/0.5–2 h (Figs. 4a–c and 5a–f) and 1300 °C/0.5 h (Figs. 4e and 5i–j) are similar, which, however, are different from those oxidized at 1200 °C/4 h (Figs. 4d and 5g–h) and 1300 °C/1 h (Figs. 4f and 5k–l). The cross-section view in Fig. 4a–c, e exhibits four layers with distinct contrasts, while five different layers are observed in Fig. 4d, f.

To further investigate the compositions and element distributions of the different layers after oxidation, EDS point and area mapping analyses were employed. The results of point composition analysis within different layers in Fig. 4c, d are illustrated in Supplementary Table 1. For the four-layer structures, EDS point analysis (1 in Fig. 4c) shows that the atomic ratio of O/Cr in the outmost layer is pretty close to the

stoichiometry of that of Cr_2O_3 , in coincidence with the XRD results. The layer below Cr_2O_3 is the unreacted Cr layer, but some Zr atoms are found to diffuse into the Cr layer, as illustrated in Supplementary Figure 7a and Supplementary Table 1 (Point 3). According to the EDS results, it is evident that the Zr atoms diffused into the Cr are quite low and the Zr atom distribution is also non-uniform. The Cr_2O_3 layer is obviously dense, with some voids only located at the out surface of Cr_2O_3 . The Cr_2O_3 layer is well bonded with the Cr coating. The main elements in the third layer are Cr and Zr, which is the inter diffusion layer of Cr and Zr. Few Nb and Fe atoms also exist. This layer is formed due to Cr–Zr inter-diffusion, and it seems that the diffusion layer is mainly $\text{Zr}(\text{Cr},\text{Fe})_2$ intermetallic³⁸ according to the Cr/Zr and Cr–Zr phase diagram³⁹. The content of Fe is too low to detect via EDS analysis in the Zr substrate. However, ~5 at.% Fe exists in the Cr–Zr diffusion layer, which indicates Fe element will gather into this layer. The oxygen content in the inner layer is about 20 at.% at point 4 in Fig. 4c. In a word, the four layers of samples oxidized at 1200 °C/2 h from outer to inner are Cr_2O_3 , Cr, Cr–Zr and $\alpha\text{-Zr}(\text{O})$ in turn.

For the five-layer structures, a ZrO_2 layer exists between the Cr–Zr diffusion layer and the substrate $\alpha\text{-Zr}(\text{O})$ layer, as shown in Fig. 4d, f. Except for the ZrO_2 layer, other layers are nearly the same as those in the aforementioned four-layer structures, as shown in Supplementary Figure 7b and Supplementary Table 1. Nevertheless, the forming process of Cr layers is somewhat different, which will be discussed later. The thickness of Cr_2O_3 , Cr, Cr–Zr and ZrO_2 layers in these samples oxidized at different temperatures and oxidation time was summarized and compared in Table 1. One interesting phenomenon can be found that the

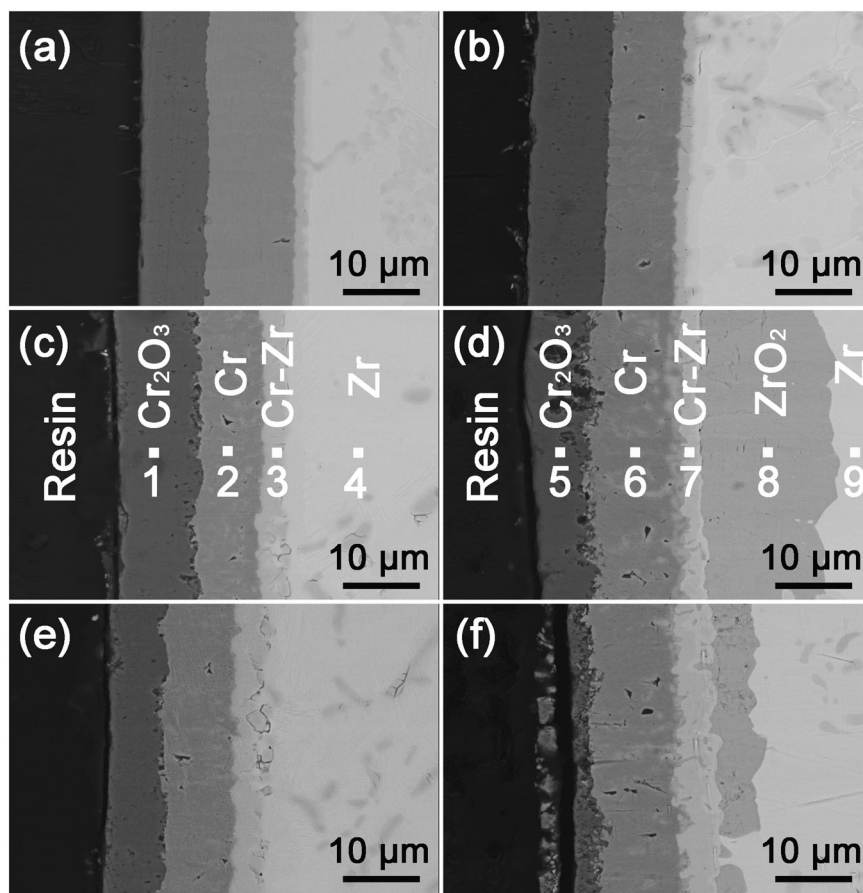


Fig. 4 Cross-sectional SEM images of the outer surface of Cr-coated Zr tube oxidized at different conditions. **a, b** 1200 °C/0.5 h, **c, d** 1200 °C/1 h, **e, f** 1200 °C/2 h, **g, h** 1200 °C/4 h, **i, j** 1300 °C/0.5 h, **k, l** 1300 °C/1 h.

thickness of Cr_2O_3 layer increased and the thickness of Cr decreased when oxidation time was raised from 0.5 to 2 h at 1200 °C. However, the inverse variation trends were observed when the oxidation time was further increased to 4 h. The reasons are associated with different oxidation processes and oxidation mechanisms that will be rationalized later. Similarly, the thickness of Cr_2O_3 decreased and the thickness of Cr increased from 0.5 to 1 h at 1300 °C. However, compared with the oxidation results, the oxidation rate at 1300 °C is much faster than at 1200 °C, in agreement with the weight gain results (Supplementary Fig. 1). The Zr substrate is to be oxidized when the exposure time is longer than 2 h at 1200 °C. While at 1300 °C, the Zr substrate is oxidized within 1 h exposure. Besides, the Cr–Zr interdiffusion rate at 1300 °C is also faster than at 1200 °C.

Structural characterization of the interfaces

See Fig. 4d, the contrast of interface between Cr and Cr–Zr layers indicates that the compositions of the sample oxidized in 1200 °C for 4 h are complicated. TEM was used to analyze the microstructures and compositions at the interface of layers 5/6, 6/7, and 7/8 (Fig. 4d) respectively, and the results are shown in Figs. 6, 7, and 8. In Fig. 6, we can find the Cr_2O_3 and Cr layers and corresponding interface, which is in good agreement with the SEM and EDS results (Figs. 4 and 5).

A high angle annular dark-field (HAADF) image at the interface of layers 6/7 is displayed in Fig. 7a. The contrasts indicate that there are three different sublayers. The outer sublayer consists of Zr and O elements and the selected area electron diffraction (SAED) pattern (Fig. 7e) indicates a structure of ZrO_2 . The inner

layer contains Zr, Cr, and Fe elements, and the proportion of Zr and Cr is nearly 1:2 (at.%). Based on the SAED pattern, this sublayer can be concluded as $\text{Zr}(\text{Cr},\text{Fe})_2$. For the middle sublayer, the thickness is about 200–500 nm and the elements include Zr, Cr, Fe, and O. Although the SAED pattern indicates crystalline grains (for example grain 2 in Fig. 7d), the crystal structure of the present ZrCrFeO layer can not be determined according to the limited results. More detailed work should be performed in the future.

Figure 8a shows a representative HAADF image at the interface of layers 7/8 in Fig. 4d. The elemental composition and content are the same as the inner layer in Fig. 7a. This layer is also $\text{Zr}(\text{Cr},\text{Fe})_2$ and the main phase of the Cr–Zr layer is $\text{Zr}(\text{Cr},\text{Fe})_2$, as demonstrated in SEM and EDS results mentioned above (Figs. 4d and 5b). A combined EDS and SAED analyses (Fig. 8c and f) reveal that the inner layer is ZrO_2 . Besides, a discontinuous layer exists between the layers of $\text{Zr}(\text{Cr},\text{Fe})_2$ and ZrO_2 . Some existing particles are proved to be Cr by EDS and SAED pattern (Fig. 8b, c, and e). The formation of Cr particles is attributed to a chemical reaction as described by Reaction 4 (the slight contribution of Fe is neglected)³⁸.



In present work, the Gibbs free energy ($\Delta_r G_{\text{m},\text{B}}^\ominus$) of Reaction 4 was calculated. We first find $\Delta_r G_{\text{m},\text{B}}^\ominus$ values of ZrCr_2 , O, ZrO_2 , and Cr, which can be found in <Langes Chemistry Handbook> that the $\Delta_r G_{\text{m},\text{B}}^\ominus$ values of O, ZrO_2 , and Cr are $231.7 \text{ kJ mol}^{-1}$, -1042 , and 0 kJ mol^{-1} , respectively. However, the $\Delta_r G_{\text{m},\text{B}}^\ominus$ value of ZrCr_2 , as intermetallic compound, can hardly be found in the handbook or literatures. Therefore, we calculate the $\Delta_r G_{\text{m},\text{B}}^\ominus$ value of ZrCr_2 before

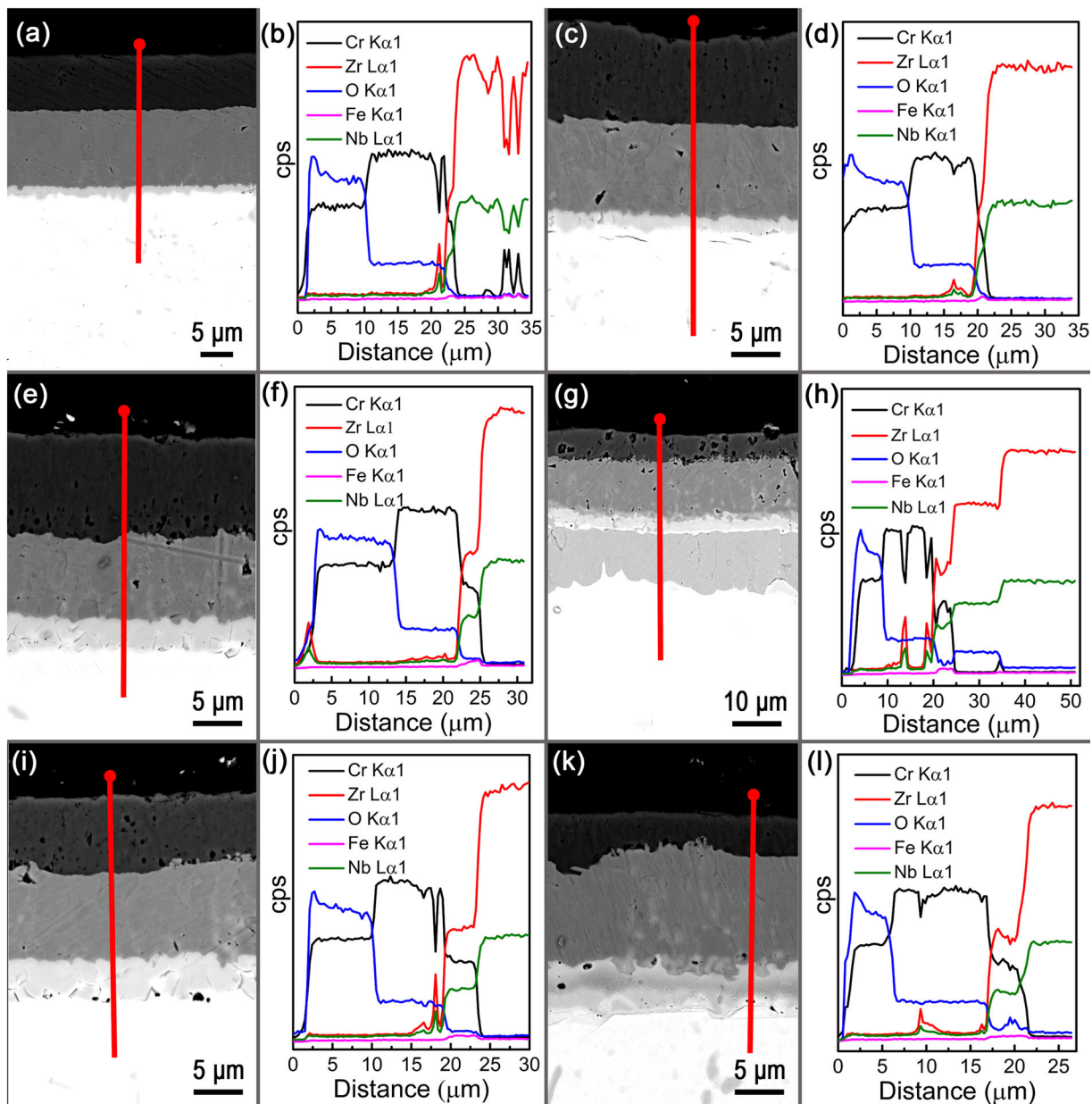


Fig. 5 Cross-sectional SEM images and corresponding EDS line scan of the outer surface of Cr-coated Zr tube oxidized at different conditions. **a, b** 1200 °C/0.5 h, **c, d** 1200 °C/1 h, **e, f** 1200 °C/2 h, **g, h** 1200 °C/4 h, **i, j** 1300 °C/0.5 h, **k, l** 1300 °C/1 h.

calculating the Gibbs free energy of Reaction 4. The calculation process is as follow:

(1) Calculate the $\Delta_f H_m^\ominus$ value of $ZrCr_2$ according to the OQMD database (Eq. 5)

$$\Delta_f H_m^\ominus = -0.036 \frac{eV}{atom} = -0.036 \times 3 \times 1.602 \times 10^{-19} \times 6.02 \times 10^{23} \text{ J mol}^{-1} = -10.417 \text{ kJ mol}^{-1} \quad (5)$$

(2) Calculate the $\Delta_f G_{m,B}^\ominus$ value of $ZrCr_2$ according to Eq. 6. As the entropy of most intermetallic compound is $<0.062 \text{ kJ K}^{-1} \text{ mol}^{-1}$, it can be considered that

$$\Delta_f G_{m,B}^\ominus \approx \Delta_f H_m^\ominus = -10.417 \text{ kJ mol}^{-1} \quad (6)$$

$$\Delta_f G_{m,B}^\ominus = \Delta_f H_m^\ominus - T\Delta_f S_m^\ominus$$

(3) Calculate Gibbs free energy ($\Delta_r G_m^\ominus$) according to Eq. 7.

$$\begin{aligned} \Delta_r G_m^\ominus &= -\Delta_f G_m^\ominus(Zr(Cr)_2, s) - 2 \times \Delta_f G_m^\ominus(O, s) + \Delta_f G_m^\ominus(Zr(O)_2, s) \\ &\quad + 2 \times \Delta_f G_m^\ominus(Cr, s) \\ &= -(-10.417 \text{ kJ mol}^{-1}) - 2 \times 231.7 \text{ kJ mol}^{-1} \\ &\quad + (-1042.8 \text{ kJ mol}^{-1}) + 2 \times 0 \\ &= -1495.783 \text{ kJ mol}^{-1} \end{aligned} \quad (7)$$

The Gibbs free energy of Reaction 4 is a negative number, which indicates the feasibility of this reaction.

As talked above, for the Cr coating oxidized at 1200 °C for 4 h, the layers from outer to inner are Cr_2O_3 , Cr(outer), ZrO_2 (outer), $ZrCrFeO$, $Zr(Cr, Fe)_2$, Cr(inner), ZrO_2 (inner) and Zr in turn. In

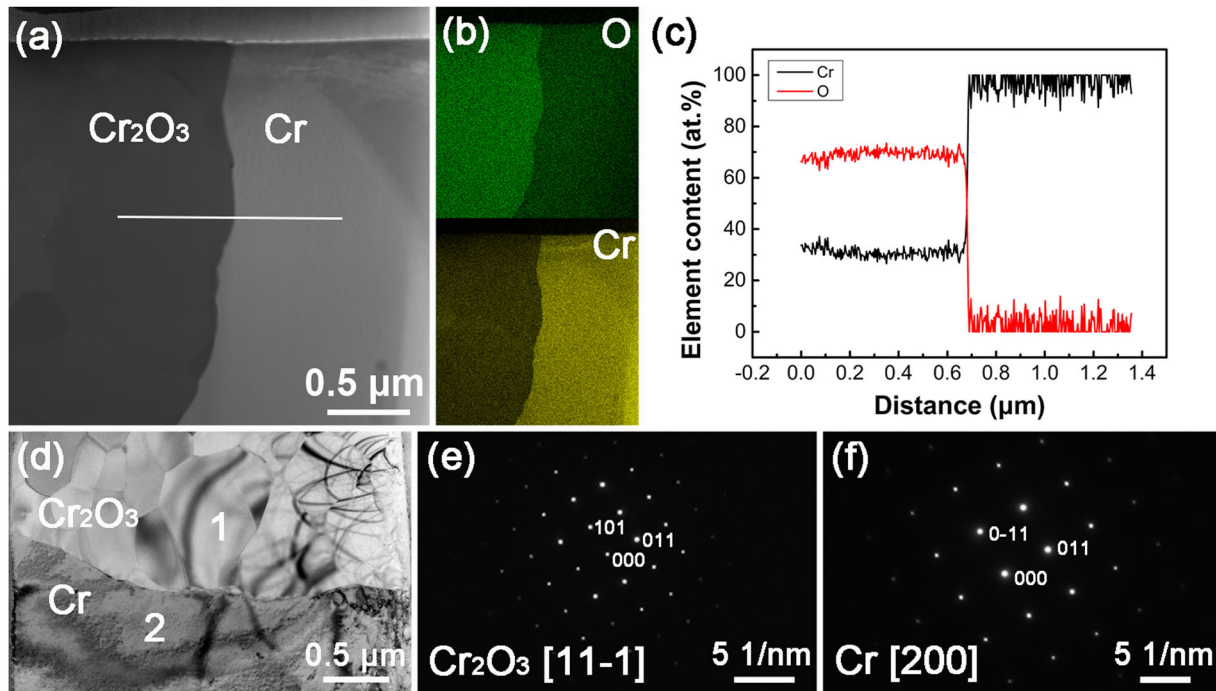


Fig. 6 Microstructures and compositions at the interface of layers 5/6 in Fig. 4. **a** HAADF and **d** TEM images of the Cr_2O_3 and Cr, and corresponding **b** EDS mappings and **c** EDS line scan, SEAD patterns of the **e** Cr_2O_3 and **f** Cr.

particular, the ZrO_2 (outer), ZrCrFeO , and Cr(inner) layers are relatively thin and discontinuous.

DISCUSSION

Oxidation kinetics of the Cr-coated Zr claddings was quantified. As the Cr coating was produced only on the outer surface of the Zr tube, the weight gain of the one-side Cr-coated Zr cannot reflect the true oxidation rate of the Cr coating/Zr substrate system. Alternatively, the oxidation kinetics was evaluated by measuring the oxides thickness. For this purpose, the SEM results was utilized to calculate the oxidation kinetics of the Cr-coated Zr at 1200 °C.

For pure Zr cladding tested at high-temperature steam environments^{40–42}, all the previous investigations showed that the oxidation kinetics could be described by a parabolic law (exponent $n \approx 0.5$). However, the oxidation of Cr in high-temperature steam was different in different works. Brachet et al.⁴³ reported a parabolic law (exponent $n \approx 0.5$); and Yeom et al.³⁴ observed quartic oxidation kinetics (exponent $n \approx 0.25$) for cold spray Cr coatings tested at 1230 °C and 1310 °C. However, Birks et al.⁴⁴ suggested that the growth of Cr during the oxidation process followed a logarithmic law.

A typical power rate equation (Eq. 8) is adopted in this work.

$$d = kt^n, \quad (8)$$

$$\ln(d) = n \ln(t) + \ln(k), \quad (9)$$

where d is the thickness of oxides (Cr_2O_3 in the outer surface and ZrO_2 in the inner surface), n is an exponent, k is a rate constant and t is the oxidation exposure time. Following this treatment, the experimental results are plotted in Fig. 9a. The value of n and k is evaluated and listed in Supplementary Table 2. The value of the correlation coefficient ($R^2 = 0.99297$) indicates that the experimental Zr oxidation results fit well with the kinetics equation (Fig. 9b). The n value of $\approx 1/2$ hints that the Zr oxidation follows parabolic kinetics, indicative of a diffusion-

controlled mechanism. This is similar to previous reports^{40–42}. However, the rate constant ($k = 146.9 \mu\text{m h}^{-0.52}$) is large, the oxidation rate (or the growth of ZrO_2 layer) of Zr is quite fast. For Cr coating, a low R^2 value (0.95336) means that the Eq. (8) fits broadly with the experimental results. The n value of ≈ 0.14 is lower than Brachet et al.'s⁴³ and Yeom et al.'s³⁴ reports. These calculations indicate that the oxidation kinetics of Cr coating does not follow a parabolic or quartic law perfectly. Then the Cr_2O_3 oxidation growth at 1200 °C was further evaluated by following the logarithmic kinetics:

$$d = k \ln(t) + A, \quad (10)$$

where d is the thickness of Cr_2O_3 , k is the rate constant, t is the oxidation exposure time and A is a constant. Figure 9b shows a comparison between experimental results and the kinetics curve derived from Eq. (10). A greater R^2 value of 0.96761 means Eq. (10) should be more applicable to present Cr_2O_3 growth. In this case, k and A for the Cr layer oxidized to Cr_2O_3 at 1200 °C are $1.3 \mu\text{m} \ln(\text{h})^{-1}$ and $9.37 \mu\text{m}$, respectively. As discussed above, the Cr coatings followed logarithmic kinetics more likely at 1200 °C water steam environments in this work. The results indicate that the growth of Cr_2O_3 should be governed by a diffusion-limited growth mechanism, which is the same as the growth of Zr layers. However, the rate constant of Cr is much lower than that of Zr, the oxidation rate of the Cr coating is therefore quite lower when in comparison with that of the Zr.

Recall that the Cr and Zr could inter-diffused to form a Cr-Zr layer. A growth model of this layer was proposed by referring to Fick's first law. The relationship between the thickness of Cr-Zr layer and the exposure time could be given below:

$$d^2 = \frac{2D_{\text{Cr-Zr}}\Delta X(X_{\text{Zr}} - X_{\text{Cr}} - \Delta X)}{(X_{\text{Zr}} - X_{\text{Zr}'})(X_{\text{Cr}'} - X_{\text{Cr}})} t \quad (11)$$

where d is the Cr-Zr layer thickness, t is the exposure time, $D_{\text{Cr-Zr}}$ is the diffusion coefficient of Zr in this layer, X_{Zr} is the content of

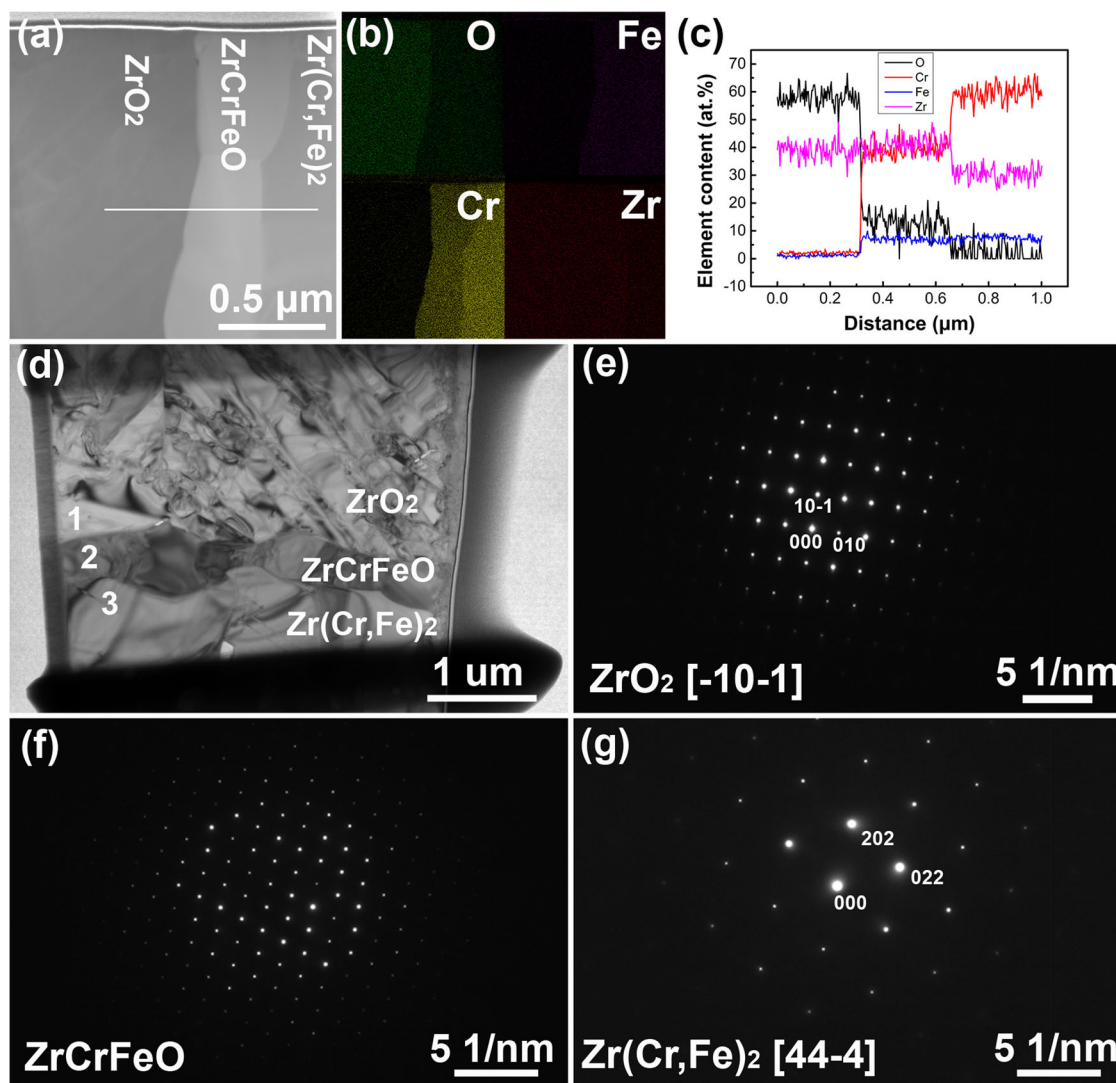


Fig. 7 Microstructures and compositions at the interface of layers 6/7 in Fig. 4. **a** HAADF and **d** TEM images of ZrO_2 , ZrCrFeO , and $\text{Zr}(\text{Cr,Fe})_2$, and corresponding **b** EDS mappings and **c** EDS line scan; SEAD patterns of **e** ZrO_2 , **f** ZrCrFeO , and **g** $\text{Zr}(\text{Cr,Fe})_2$.

Zr in the Zr layer (100 at.%), X_{Cr} is the content of Zr in the Cr layer (0 at.%), X_{Zr} is the content of Zr in the interface of Zr and Cr–Zr layers, which is the highest content of Zr in Cr–Zr layer, $X_{\text{Cr}'}$ is the content of Zr in the interface of Cr and Cr–Zr, which is the lowest content of Zr in Cr–Zr layer, $\Delta X = X_{\text{Zr}} - X_{\text{Cr}'}$. In the present work, we use the data of Cr-coated Zr oxidized at 1200 °C for 2 h, where d and t are 3.6 μm and 2 h, respectively, as shown in Table 1. X_{Zr} and $X_{\text{Cr}'}$ are 60 and 50 at.% according to the EDS results. It should be emphasized that the values of X_{Zr} and $X_{\text{Cr}'}$ are not accurate and the content of O is ignored for simplification. We just use these values to simply estimate the growth law of the Cr–Zr layer. Taking $D_{\text{Cr-Zr}}$ as $\sim 6.6 \mu\text{m}^2 \text{h}^{-1}$, the dependence of Cr–Zr layer thickness (d) on exposure time (t) was quantitatively calculated, as shown in Fig. 9d to compare with the experimental results. One can see that the experimental results agree well with the growth curve. That means that the relationship between the Cr–Zr layer thickness and the exposure time, to a first approximation, follows a parabolic law, which is consistent with the growth kinetics reported for Cr/Zr diffusion couples by Xiang et al.⁴⁵

At this point, the oxidation process can be summarized as follows. Firstly, the Cr reacted with H_2O steam (Reaction 2) to

form Cr_2O_3 , as shown in Fig. 4, and 5. The dense Cr_2O_3 layer acts as an oxygen diffusion barrier that can greatly reduce the oxidation rate in the high-temperature steam environment. At the same time, Cr and Zr diffuse into each other, producing a Cr–Zr diffusion layer, which strongly improve the bond between the Cr coating and the Zr substrate. However, ZrCr_2 is a topologically close-packed Laves phase of the AB_2 type³⁹, which may be a brittle phase and be harmful to the ductility of the coating/cladding system. Therefore, effect of Cr–Zr layer on the mechanical properties of Cr-coated Zr claddings deserves to be investigated in detail. Secondly, the thickness of both Cr_2O_3 and Cr–Zr layers increases and the thickness of unreacted Cr decreases as increasing the oxidation time (Table 1, 1200 °C/ (0.5–2 h)). It can be concluded that Cr_2O_3 and Cr–Zr layers will approach to each other. Thirdly, Zr in the diffusion layer will reduce Cr_2O_3 to Cr and Zr itself will form ZrO_2 , as shown in Fig. 4d (Table 1, 1200 °C/4 h). Similar reduced reaction process has been reported by Han et al.¹⁹. They claimed that the Cr^{3+} ions were reduced into neutral Cr, aided by the electrons transference from Zr. As the Cr is released from Cr_2O_3 , active O^{2-} ions will diffuse and react with Zr^{2+} , producing the ZrO_2 layer. Then the processes of electron transfer, ions diffusion and

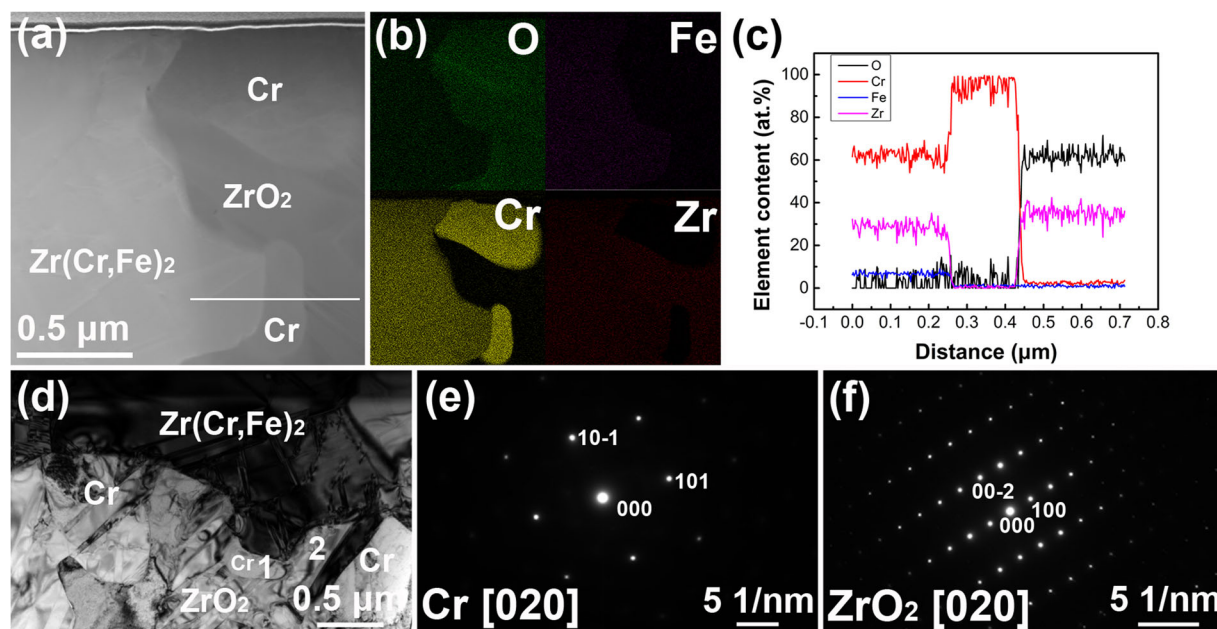


Fig. 8 Microstructures and compositions at the interface of layers 7/8 in Fig. 4. **a** HAADF and **d** TEM image of $Zr(Cr,Fe)_2$, Cr and ZrO_2 , and corresponding **b** EDS mappings and **c** EDS line scan; SEAD patterns of **e** Cr and **f** ZrO_2 .

reduction reaction repeat. As a result, the thickness of Cr and ZrO_2 layers increases, while the Cr_2O_3 layers thins. Finally, when the oxidation rate between Cr and H_2O and the reduction rate between Zr and Cr_2O_3 reach a balance, the thickness of Cr_2O_3 and Cr layers keep unchanged, while the thickness of ZrO_2 layer still increases. Therefore, the Cr layer in the four-layer samples is the original and unreacted Cr and that in the five-layer samples is a reduction product. The oxidation process of Cr-coated claddings at $1300\text{ }^\circ\text{C}$ has no obvious difference, which is not described again.

In this work, using the PVD process, Cr coatings were successfully deposited on zirconium alloy claddings with the goal of enhancing accident tolerance in light water reactors applications. Systematic studies on the oxidation behavior of Cr coated samples under high-temperature steam environment have been conducted. The results indicated that the Cr coatings showed protective ability on the Zr claddings even in the steam environments above $1200\text{ }^\circ\text{C}$. The oxidation kinetics was discussed that the oxidation of Zr substrates followed a parabolic kinetics at $1200\text{ }^\circ\text{C}$ and the oxidation was greatly accelerated. However, the oxidation of Cr coatings followed logarithmic kinetics and the oxidation rate was much slower than the Zr substrates at the same oxidation condition. The oxidation process and underlying mechanism varied when the oxidation time increased from 2 to 4 h at $1200\text{ }^\circ\text{C}$. As the oxidation time increased from 0.5 to 2 h at $1200\text{ }^\circ\text{C}$, the Cr_2O_3 and Cr–Zr layers thickened and Cr layer thinned. However, as a reduction reaction existed between Cr_2O_3 and Zr, the Cr_2O_3 layer decreased and Cr increased in thickness as the oxidation time increased further to 4 h. At the same time, the Zr substrate was oxidized and resulted in the formation of ZrO_2 . The layers from outer to inner are Cr_2O_3 , Cr, ZrO_2 , $ZrCrFeO$, $Zr(Cr, Fe)_2$, Cr, ZrO_2 and Zr in turn. The Cr layer underwent a significant variation with the oxidation process. The Cr layer in samples oxidized at $1200\text{ }^\circ\text{C}/(0.5\text{--}2\text{ h})$ and $1300\text{ }^\circ\text{C}/0.5\text{ h}$ kept unreacted. While in the samples oxidized at $1200\text{ }^\circ\text{C}/4\text{ h}$ and $1300\text{ }^\circ\text{C}/1\text{ h}$, the Cr layer was a reduction product.

METHODS

Sample preparation

Cr coatings were deposited on the outer surface of Zr-1Nb alloy claddings ($\sim 25\text{ cm}$ in length, 9.5 mm in outer diameter, and 0.57 mm in wall thickness) by using magnetron sputtering (one kind of PVD). Firstly, the tubes were ultrasonically cleaned in acetone and ethanol for 10 min, respectively. The claddings were mounted in the chamber of PVD device after drying. The chamber was evacuated down to a base pressure of 3×10^{-5} Torr, and then heated to $200\text{ }^\circ\text{C}$. Prior to depositing, the surface of Zr-1Nb alloy claddings and the Cr targets was subjected to cleaning at 175 W for 30 min and 450 W for 15 min, respectively. During the deposition process, the pressure was increased with continuously flowing Ar and the claddings were negatively biased at 70 V and rotated at a speed of 70 rpm.

Oxidation experiments

High-temperature steam oxidation tests for Cr-coated Zr tubes (1 cm in length) were conducted at $1200\text{ }^\circ\text{C}$ and $1300\text{ }^\circ\text{C}$ for different exposure times, respectively, by using a thermo-gravimetric analyzer (TGA, SETARAM, France). The Cr-coated samples used for high-temperature steam oxidation tests were cut from the longer tubes. A heating rate of $20\text{ }^\circ\text{C min}^{-1}$ was applied from room temperature (RT) to the target temperatures. The temperature was kept for the designed time and then cooled to RT naturally after the oxidation test. Water vapor of 90% RH was supplied into the chamber at the beginning of the temperature increased and the water steam flux is 50 ml min^{-1} .

Characterization of microstructures and compositions

The phase constitution of samples before and after oxidation was determined by X-ray diffraction analysis (XRD, EMPYREAN, PANalytical, Netherlands). Microstructures and compositions of the samples were examined by optical microscopy (OM, AX10, ZEISS, Germany), scanning electron microscopy (SEM, Gemini 500, ZEISS, Germany) equipped with an energy dispersion spectrometer (EDS, X-Max 80T, Oxford, UK) and transmission electronic microscopy (TEM, JEM-2100F, JEOL, Japan), respectively. Cross-sectional samples for OM and SEM analysis were inlaid with epoxy resin, and then furnished and polished via abrasive paper, diamond paste, and nanometer SiO_2 suspension. Finally, the samples were etched with an acid solution of $30HNO_3 + 30H_2SO_4 + 10HF + 30H_2O$ (vol. %) for OM analysis and deposited platinum (the thickness is $\sim 5\text{ nm}$) for SEM analysis, respectively. TEM specimens were prepared using Focused Ion Beam (FIB, Helios 600i, FEI, USA).

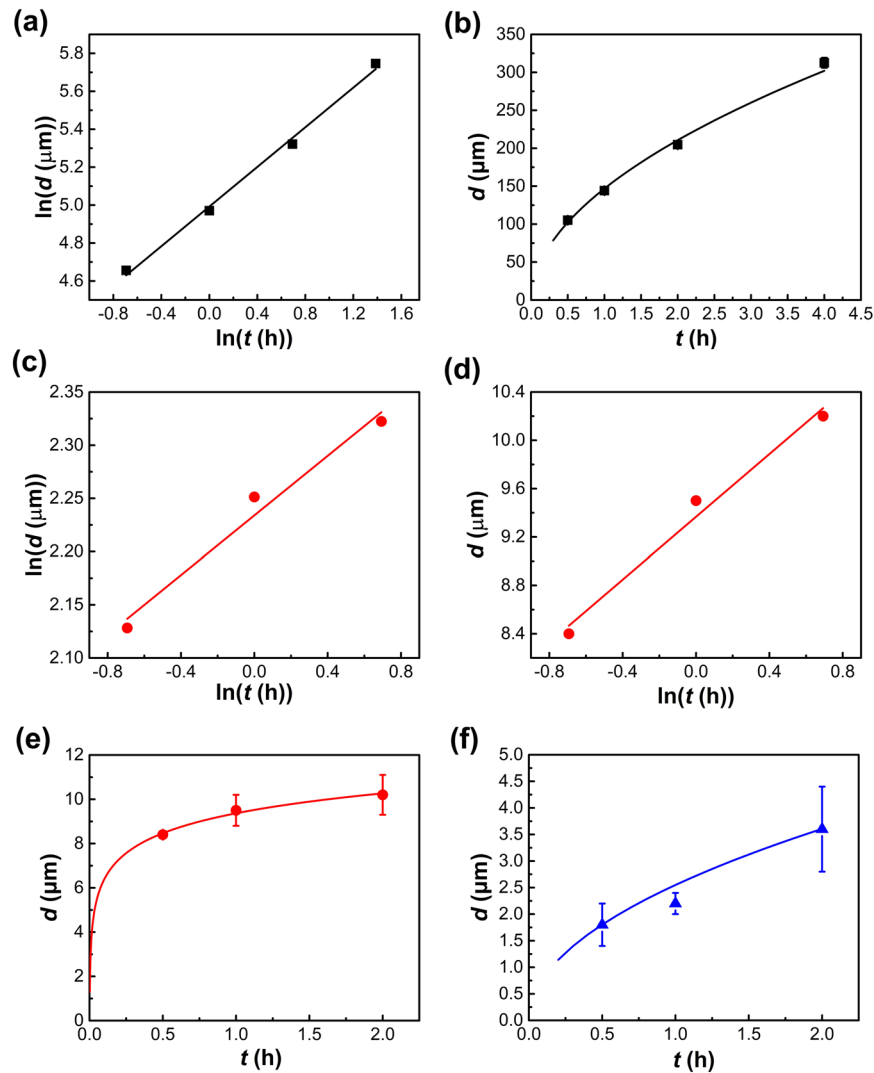


Fig. 9 Oxidation kinetics analysis of Zr and Cr. **a** Logarithm of the thickness of **a** ZrO_2 and **c** Cr_2O_3 versus the logarithm of oxidation time; thickness of **d** Cr_2O_3 versus the logarithm of oxidation time; the relationship between the thickness of **b** ZrO_2 , **e** Cr_2O_3 , **f** Cr-Zr layers and the oxidation time.

DATA AVAILABILITY

The datasets generated and/or analyzed during the current study are available from the corresponding author upon reasonable request.

Received: 2 October 2020; Accepted: 15 January 2021;

Published online: 12 February 2021

REFERENCES

- Zinkle, S. J., Terrani, K. A., Gehin, J. C., Ott, L. J. & Snead, L. L. Accident tolerant fuels for LWRs: A perspective. *J. Nucl. Mater.* **448**, 374–379 (2014).
- Brachet, J. C., Lorrette, C., Michaux, A., Sauder, C. & Ambard, A. CEA studies on advanced nuclear fuel claddings for enhanced Accident Tolerant LWRs Fuel (LOCA and beyond LOCA conditions). Fontevraud 8-Contribution of Materials Investigations and Operating Experience to LWRs' Safety, Performance and Reliability France, Avignon, (2014).
- Koo, Y. H. et al. KAERI'S development of LWR accident-tolerant fuel. *Nucl. Technol.* **186**, 295–304 (2014).
- Murase, K., Murase, J., Horie, R. & Endo, K. Effects of the Fukushima Daiichi nuclear accident on goshawk reproduction. *Sci. Rep.* **5**, 9405 (2015).
- Sowder, A. G. Challenges and opportunities for commercialization of enhanced accident tolerant fuel for light water reactors: a utility-in-formed perspective. IAEA TECDOC Series, **119** (2016).
- James, A. The fourth generation of nuclear power. *Prog. Nucl. Energy* **40**, 301–307 (2002).
- Zhong, W., Mouche, P. A., Han, X., Heuser, B. J. & Was, G. S. Performance of iron-chromium-aluminum alloy surface coating on Zircaloy 2 under high-temperature steam and normal BWR operating conditions. *J. Nucl. Mater.* **470**, 327–338 (2015).
- Maier, B. R. et al. Cold spray deposition of Ti_2AlC coatings for improved nuclear fuel cladding. *J. Nucl. Mater.* **466**, 712–717 (2015).
- Usui, T. et al. SiC coating as hydrogen permeation reduction and oxidation resistance for nuclear fuel cladding. *J. Nucl. Sci. Technol.* **52**, 1318–1322 (2015).
- Cheng, B., Kim, Y. J. & Chou, P. Improving accident tolerance of nuclear fuel with coated Mo-alloy cladding. *Nucl. Eng. Technol.* **48**, 16–25 (2016).
- Yamamoto, Y. et al. Development and property evaluation of nuclear grade wrought FeCrAl fuel cladding for light water reactors. *J. Nucl. Mater.* **467**, 703–716 (2015).
- Yano, Y. et al. Ultra-high temperature tensile properties of ODS steel claddings under severe accident conditions. *J. Nucl. Mater.* **487**, 229–237 (2017).
- Unocic, K. A., Yamamoto, Y. & Pint, B. A. Effect of Al and Cr content on air and steam oxidation of FeCrAl alloys and commercial APMT alloy. *Oxid. Met.* **87**, 431–441 (2017).
- Deck, C. P. et al. Characterization of SiC–SiC composites for accident tolerant fuel cladding. *J. Nucl. Mater.* **466**, 667–681 (2015).
- Lee, Y., No, H. C. & Lee, J. I. Design optimization of multi-layer silicon carbide cladding for light water reactors. *Nucl. Eng. Des.* **311**, 213–223 (2017).

16. Koyanagi, T. & Katoh, Y. Mechanical properties of SiC composites neutron irradiated under light water reactor relevant temperature and dose conditions. *J. Nucl. Mater.* **494**, 46–54 (2017).
17. Maier, B. et al. Development of cold spray chromium coatings for improved accident tolerant zirconium-alloy cladding. *J. Nucl. Mater.* **519**, 247–254 (2019).
18. Kim, H. G., Yang, J. H., Kim, W. J. & Koo, Y. H. Development status of accident-tolerant fuel for light water reactors in Korea. *Nucl. Eng. Technol.* **48**, 1–15 (2016).
19. Han, X. C., Xue, J. X., Peng, S. M. & Zhang, H. B. An interesting oxidation phenomenon of Cr coatings on Zry-4 substrates in high temperature steam environment. *Corros. Sci.* **156**, 117–124 (2019).
20. Wei, T. G. et al. Microstructure, corrosion resistance and oxidation behavior of Cr-coatings on Zircaloy-4 prepared by vacuum arc plasma deposition. *Corros. Sci.* **158**, 108077 (2019).
21. Gil, K. H. et al. Out-of-pile performance of surface-modified Zr cladding for accident tolerant fuel in LWRs. *J. Nucl. Mater.* **510**, 93–99 (2018).
22. Han, X. C., Wang, Y., Peng, S. M. & Zhang, H. B. Oxidation behavior of FeCrAl coated Zry-4 under high temperature steam environment. *Corros. Sci.* **149**, 45–53 (2019).
23. Tunes, M. A., Vishnyakov, V. M. & Donnelly, S. E. Synthesis and characterisation of high-entropy alloy thin films as candidates for coating nuclear fuel cladding alloys. *Thin Solid Films* **649**, 115–120 (2018).
24. Tang, C. C., Stueber, M., Seifert, H. J. & Steinbrueck, M. Protective coatings on zirconium-based alloys as accident-tolerant fuel (ATF) claddings. *Corros. Rev.* **35**, 141–165 (2017).
25. Duan, Z. et al. Oxidation and electrochemical behaviors of Al₂O₃ and ZrO₂ coatings on Zircaloy-2 cladding by thermal spraying. *Surf. Coat. Technol.* **334**, 319–327 (2018).
26. Tang, C. C. et al. Deposition, characterization and high-temperature steam oxidation behavior of single-phase Ti₂AlC-coated Zircaloy-4. *Corros. Sci.* **135**, 87–98 (2018).
27. Arias, D. & Abriata, J. P. The Cr–Zr (Chromium–Zirconium) system. *Bull. Alloy Phase Diagrams* **7**, 237–244 (1986).
28. Brachet, J. C. et al. Behavior of chromium coated M5™ claddings under LOCA conditions. *Proc. WRRFPM Conference* (Jeju, 2017).
29. Oelrich, R. et al. Overview of Westinghouse lead accident tolerant fuel program. *Proc. TopFuel Conference 2018* (Prague, 2018).
30. Bischoff, J. et al. Cr-coated cladding development at Framatome. *Proc. TopFuel Conference 2018* (Prague, 2018).
31. Lin, Y., Faucett, R., Desilva, S., Lutz, D. & Yilmaz, M. Path toward industrialization of enhanced accident tolerant fuel. *Proc. TopFuel Conference 2018* (Prague, 2018).
32. Park, J. H. et al. High temperature steam-oxidation behavior of arc ion plated Cr coatings for accident tolerant fuel claddings. *Surf. Coat. Technol.* **280**, 256–259 (2015).
33. Shahin, M. et al. Experimental investigation of cold-spray chromium cladding. *Proc. TopFuel Conference 2018* (Prague, 2018).
34. Yeom, H. et al. High temperature oxidation and microstructural evolution of cold spray chromium coatings on Zircaloy-4 in steam environments. *J. Nucl. Mater.* **526**, 151737 (2019).
35. Othman, N. K., Othman, N., Zhang, J. & Young, D. J. Effects of water vapour on isothermal oxidation of chromia-forming alloys in Ar/O₂ and Ar/H₂ atmospheres. *Corros. Sci.* **51**, 3039–3049 (2009).
36. Hänsel, M., Quadackers, W. J. & Young, D. J., Role of water vapor in chromia-scale growth at low oxygen partial pressure. *Oxid. Met.* **59**, 285–301 (2003).
37. Arifin, S. K., Hamid, M., Berahim, A. N. & Ani, M. H. Effects of water vapor on protectiveness of Cr₂O₃ scale at 1073 K. *Mater. Sci. Eng.* **290**, 012085 (2018).
38. Massalski, T. B., Okamoto, H., Subramanian, P. R. & Kacprzak, L. *Binary Alloy Phase Diagrams*. (ASM International, 1990).
39. Brachet, J. C. et al. High temperature steam oxidation of chromium-coated zirconium-based alloys: Kinetics and process. *Corros. Sci.* **167**, 108537 (2020).
40. Baek, J. H., Park, K. B. & Jeong, Y. H. Oxidation kinetics of Zircaloy-4 and Zr-1Nb-15n-0.1Fe at temperature of 700–1200°C. *J. Nucl. Mater.* **335**, 443–456 (2004).
41. Sawarn, T. K., Banerjee, S., Samanta, A., Rath, B. N. & Kumar, S. Study of oxide and α-Zr(O) growth kinetics from high temperature steam oxidation of Zircaloy-4 cladding. *J. Nucl. Mater.* **467**, 820–831 (2015).
42. Cathcart, J. V. et al. *Zirconium Metal-Water Oxidation Kinetics. IV. Reaction Rate Studies. [BWR:PWR]*. (Oak Ridge National Laboratory, 1977).
43. Brachet, J. C. et al. Early studies on Cr-coated Zircaloy-4 as enhanced accident tolerant nuclear fuel claddings for light water reactors. *J. Nucl. Mater.* **517**, 268–285 (2019).
44. Birks, N., Meier, G. H. & Pettit, F. *Introduction to the High Temperature Oxidation of Metals*, 2nd edn. (Cambridge University Press, 2006).
45. Xiang, W. X. & Ying, S. H. Study on reaction diffusion of Zircaloy-2/Chromium system. *Nucl. Power Eng.* **23**, 34–39 (2002).

ACKNOWLEDGEMENTS

The work was supported financially by grants from the National Key R&D Program of China (No.2017YFB0702404) and CGN Innovation Strategic Project (No. 3100069733 and 3100102354).

AUTHOR CONTRIBUTIONS

H.-B.M. designed the experiments, performed the microstructures and compositions analysis, and wrote the paper. J.Y. and Y.-H.Z. contributed to the experiments of high-temperature water steam oxidation. J.-D.Z. contributed to the calculation of diffusion of Cr–Zr layers. M.-Y.Y. contributed to the sample preparation for OM and TEM analysis. T.L., Q.-S.R., Y.-H.L. and G.L. revised the paper. All the authors contributed to the interpretation of the experimental data and discussed the results.

COMPETING INTERESTS

The authors declare no competing interests.

ADDITIONAL INFORMATION

Supplementary information The online version contains supplementary material available at <https://doi.org/10.1038/s41529-021-00155-8>.

Correspondence and requests for materials should be addressed to T.L. or G.L.

Reprints and permission information is available at <http://www.nature.com/reprints>

Publisher's note Springer Nature remains neutral with regard to jurisdictional claims in published maps and institutional affiliations.



Open Access This article is licensed under a Creative Commons Attribution 4.0 International License, which permits use, sharing, adaptation, distribution and reproduction in any medium or format, as long as you give appropriate credit to the original author(s) and the source, provide a link to the Creative Commons license, and indicate if changes were made. The images or other third party material in this article are included in the article's Creative Commons license, unless indicated otherwise in a credit line to the material. If material is not included in the article's Creative Commons license and your intended use is not permitted by statutory regulation or exceeds the permitted use, you will need to obtain permission directly from the copyright holder. To view a copy of this license, visit <http://creativecommons.org/licenses/by/4.0/>.

© The Author(s) 2021